



Microstructural effects on ductile fracture in heterogeneous materials. Part II: Applications to cast aluminum microstructures

Daniel Paquet, Somnath Ghosh *

Department of Mechanical Engineering, The Ohio State University, 201 West 19th Avenue, Columbus, OH 43210, United States

ARTICLE INFO

Article history:

Available online 22 July 2010

Keywords:

Rate-dependent ductile fracture
Heterogeneous materials
Actual microstructure
LE-VCFEM

ABSTRACT

This is the second of a two part paper aimed at investigating the effects of microstructural morphology, material properties and loading on rate-dependent ductile fracture of heterogeneous materials. The *locally enhanced Voronoi cell finite element method* (LE-VCFEM) is used for micromechanical analyses of deformation and failure in complex microstructural volume elements. The first part of this paper sequence evaluates the sensitivity of strain to failure of computer simulated microstructures to loading rate, microstructural morphology and material properties. In this second part, LE-VCFEM simulations of actual microstructures of a cast aluminum alloy micrograph are used to validate a strain to failure model developed in the first part. A method for identification of critical regions within a heterogeneous microstructure is also developed and validated using in-situ observations of a two-point bending test. The influence of applied strain rates on ductile fracture of micrograph-based complex microstructures is also investigated.

© 2010 Elsevier Ltd. All rights reserved.

1. Introduction

Heterogeneous ductile materials such as cast aluminum alloys and metal matrix composites (MMC's) are widely used in the automotive and aerospace industry. High performance applications in structural components put considerable demands on their mechanical properties such as stiffness, strength, toughness and ductility. Many of these materials possess reasonable strengths and stiffnesses and they improve the performance-to-weight ratio of the structural components. However, as designs become more complex and the power output requirements increase, practical limits of their ductility and ultimate strength are being reached. A concern that arises is that, even with minor variability, processes could lead to parts that do not meet ductility requirements (elongation of <1% is observed in A319 alloy in the automotive industry). It is imperative to develop accurate computational models that will enable better material design to deliver enhanced properties like high ductility and strength, concurrently. The models should account for the details of microstructural morphology, as well as incorporate actual mechanisms of deformation and failure, e.g. damage nucleation by inclusion cracking, followed by damage propagation by void nucleation, growth and coalescence in the matrix. Experimental studies, e.g. in Caceres et al. [1–6], have led to limited material specific empirical models for ductility. However in general, these models cannot be extended to other materials without additional experimental testing. Morphological parameters like shape, size and spatial distribution and material properties have very pronounced effects on response, particularly on failure properties like ductility and toughness. There is a paucity of models that have been able to isolate the effects of individual characteristic parameters on these properties [4]. Nevertheless, for better material design, it is necessary to have a comprehensive knowledge of these isolated or correlated effects through realistic micromechanics models. This two part paper is an attempt to partially overcome this void.

* Corresponding author. Tel.: +1 614 292 2599; fax: +1 614 292 7369.

E-mail address: ghosh.5@osu.edu (S. Ghosh).

Nomenclature

\bar{d}	inclusion normalized size
d^*	effective size of inclusions
e_{xx}	macroscopic normal strain in x -direction
\tilde{f}	combined measure of inclusion volume fraction and clustering
V_f	inclusion volume fraction
γ_0	viscosity constant
ϵ_{fail}	strain to failure
θ	inclusion orientation
θ^*	effective orientation of inclusions
ι	cluster contour index
ρ	inclusion roundness
ρ^*	effective roundness of inclusions
Σ_{xx}	macroscopic normal stress in x -direction
GTN	Gurson–Tvergaard–Needleman
LE-VCFEM	locally enhanced Voronoi cell finite element method
MMC	metal matrix composite
SDAS	secondary dendrite arm spacing
VCFEM	Voronoi cell finite element method

In the first of this two part paper [7], detailed sensitivity analysis has been conducted in terms of various characteristic functions to investigate the effects of loading rate, specific microstructural parameters and material properties on strain to failure or ductility. Extensive micromechanical simulations of computer simulated microstructures with the powerful locally enhanced Voronoi cell finite element method (LE-VCFEM) [8] have been used to quantify the effects of these parameters on ductile fracture. The study in [7] has also developed a model that delineates the dependence of strain to failure on specific morphological functions. The second part of this paper sequence, extends the analyses to investigate the behavior of actual microstructures, acquired from cast aluminum micrographs. LE-VCFEM simulations of image-based microstructural elements containing a dispersion of inclusions of varying sizes, shapes and orientations are conducted to assess their effects on ductility. The effectiveness of the sensitivity based models developed in part I is also tested in this paper for cast aluminum microstructures. Section 2 of this paper extends the strain to failure model of [7] to actual microstructures as seen in micrographs. In Section 3, a method for the identification of critical regions in the microstructure is developed and compared to in-situ observations of a two-point bending test. The effect of applied strain rate on ductile fracture of actual microstructures is investigated in Section 4.

2. Rate-independent strain to failure of image-based microstructures

As discussed in [7], the locally enhanced VCFEM or LE-VCFEM developed in [8] can model microstructural ductile fracture due to inclusion cracking followed by void nucleation, growth and coalescence in a rate-dependent porous plastic matrix. The inclusion phase is modeled as isotropic, linear elastic. Inclusion cracking is governed by a Weibull probability distribution based initiation criterion. An elliptical crack is introduced in the inclusion when the criterion is met. The matrix phase in [7] is modeled as a rate-dependent elastic–viscoplastic material containing microscopic voids. A viscoplastic extension (see [9]) of the Gurson–Tvergaard–Needleman (GTN) model in [10–12], governs the matrix constitutive behavior.

2.1. A strain to failure model in terms of morphological parameters

Sensitivity studies in [7] have been utilized to formulate functional dependence of the strain to failure ϵ_{fail} on morphological parameters (Eq. (46) in [7]) as:

$$\epsilon_{fail} = 2.25(11.5 + 7.63 \cos \theta - 19.6 \cos^2 \theta) \frac{e^{4.38\rho}}{d^{4.14}} \left(\frac{8.63\tilde{f} - 6.94}{\tilde{f} - 0.848} \right) \times 10^{-10} \quad (1)$$

where $\tilde{f} = \frac{\iota}{0.929 - 1.83V_f}$ reflects the combined effects of clustering ι [13] and inclusion volume fraction V_f . The function assumes identical inclusions (roundness ρ and normalized size \bar{d}) and identical orientations θ . The predictive model (1) is tested for strain to failure in actual microstructures.

Direct application of Eq. (1) is inappropriate for complex image-based microstructural domains constructed from micrographs of heterogeneous metals or alloys like cast aluminum, which contain inclusions of varying sizes, shapes and orientations. Also, the formula for random orientations in Eq. (47) in [7] does not work since the orientations of large inclusions have stronger influence on the strain to failure. Consequently, effective shape, orientation and size parameters

denoted by ρ^* , θ^* and d^* are introduced for the image-based complex microstructures. Weighted averages of the roundness, orientation, and size, with weights proportional to the influence on ϵ_{fail} leads to effective parameters as:

$$\rho^* = \frac{\sum w_i \rho_i}{\sum w_i}, \quad \theta^* = \frac{\sum w_i |\theta_i|}{\sum w_i}, \quad (d^*)^2 = \frac{\sum w_i (\bar{d}_i)^2}{\sum w_i} \quad (2)$$

where the sum is performed over all inclusions in the microstructural domain. Large inclusions oriented along the loading axis have higher weights and hence, the weighting function is defined as $w_i = (\bar{d}_i)^n \cos \theta_i$. The exponent is set to $n = 4.14$ based on sensitivity studies in [7]. d^* is used for the effective size, since the Weibull crack initiation criterion depends on the area of inclusions (2D), i.e. $v \sim \bar{d}^2$. The absolute value of orientation with respect to the loading axis $\theta \in [-90^\circ, 90^\circ]$ is introduced due to symmetry. Thus the modified strain to failure equation with effective parameters becomes:

$$\epsilon_{fail} = 2.25(11.5 + 7.63 \cos \theta^* - 19.6 \cos^2 \theta^*) \frac{e^{4.38\rho^*}}{d^{*4.14}} \left(\frac{8.63\tilde{f} - 6.94}{\tilde{f} - 0.848} \right) \times 10^{-10} \quad (3)$$

2.2. Strain to failure predictions for a cast aluminum alloy A356

Fig. 1 shows a micrograph of a cast aluminum alloy A356 from Ford Research Laboratory (FRL). This alloy belongs to the family of Al–Si–Mg hypoeutectic casting alloys. These alloys have a microstructure that comprises of: (i) age-hardened aluminum matrix, strengthened by Mg/Si and Si precipitates and (ii) a dispersion of Si inclusions resulting from the eutectic reaction [2]. The microstructure is composed of two phases, viz. the aluminum-rich dendrite cell matrix material and the brittle silicon inclusions located at cell boundaries. The rate of cooling in the casting process has a strong influence on the spatial dispersion of these second-phase inclusions [13]. The solidification process tends to push the silicon inclusions into the regions between the evolving secondary aluminum dendrites. Once the eutectic temperature is reached, the silicon inclusions are pinned in location. The presence of silicon manifests the boundary between two adjacent secondary aluminum dendrite arms. The distance between two arms is directly related to the cooling rate during solidification and is measured as secondary dendrite arm spacing or SDAS. In addition to affecting the SDAS, the cooling rate can also significantly affect the size, shape and distribution of silicon and intermetallic inclusions, as well as any porosity present. The microstructure in Fig. 1 has a SDAS of 30 μm .

Three regions are selected from the micrograph in Fig. 1 and are labeled as microstructural domains 1–3. Each of the three regions is characterized by a high level of inclusion clustering along the dendrite cell boundaries. A fourth microstructural domain, with a more homogeneous distribution of inclusions is also generated for comparison. Material properties used in these simulations are the same as those used for the sensitivity analysis in [7].

Morphological parameters, as well as the simulated strain to failure ϵ_{fail} , for the four microstructural domains are listed in Table 1. The parameters are volume fraction V_f , cluster contour index ι , effective roundness ρ^* , effective orientation θ^* and effective size d^* . LE-VCFEM simulation generated macroscopic stress–strain plots are shown in Fig. 2. Corresponding contour plots of the microscopic void volume fraction at failure strain are depicted in Fig. 3. The two last columns of Table 1 are the strain to failure predicted with Eq. (3) and the corresponding error between the model and numerical experiments.

The values of strain to failure predicted by Eq. (3) generally agree well with those obtained from micromechanical LE-VCFEM analyses for the microstructural domains 1, 3, and 4. The difference is slightly more for microstructural domain 2. This discrepancy can be rationalized through a close look at the macroscopic stress–strain plot and contour plot of Figs. 2

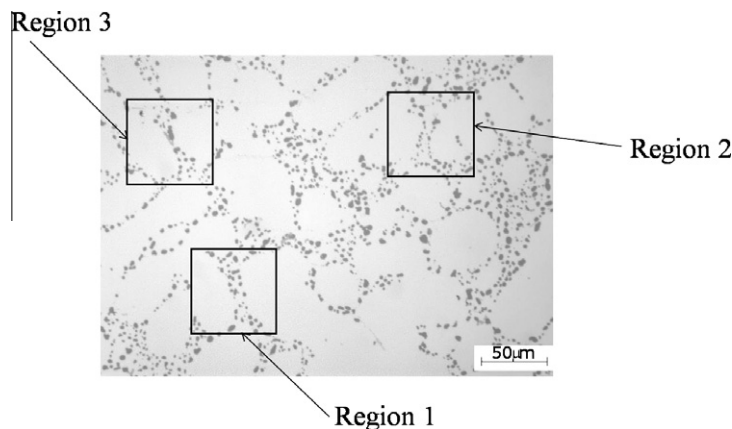
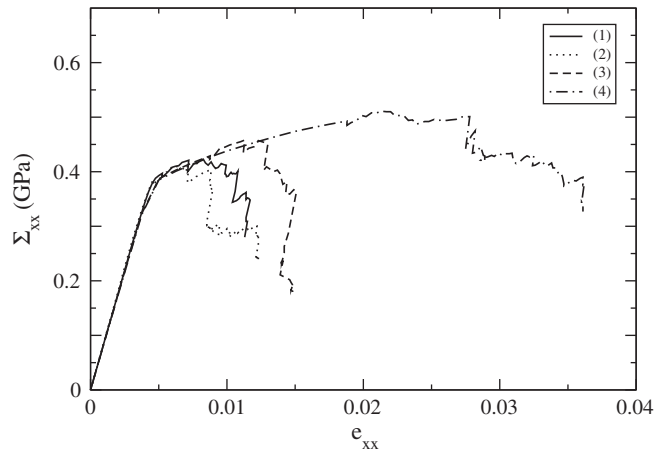


Fig. 1. Micrograph of a A356 cast aluminum alloy showing regions corresponding to the three microstructural domains (1–3) (Micrograph: Courtesy Ford Research Laboratory).

Table 1

Morphological parameters, and simulated and predicted strain to failure of four microstructural domains of a cast aluminum alloy A356.

Cases	V_f (%)	ι	ρ^*	θ^* (°)	d^*	ϵ_{fail}	Eq. (3)	Err (%)
1	7.0	0.815	0.605	34.4	0.067	0.010	0.011	10.0
2	9.0	0.828	0.645	30.3	0.071	0.011	0.008	27.3
3	6.4	0.869	0.689	47.1	0.078	0.013	0.014	7.7
4	5.8	0.816	0.652	30.0	0.051	0.036	0.033	8.3

**Fig. 2.** Macroscopic stress–strain response in uniaxial tension for four microstructural domains of a cast aluminum alloy A356.

and 3. The simulated value of ϵ_{fail} exceeds the predicted value (0.008) due to the fact that ductile cracking is arrested once it has propagated into a region free of large inclusions. This can be seen in Fig. 3b. Following crack arrest, there is intense matrix deformation which leads to a higher strain to failure. This phenomenon results in a plateau in the stress–strain curve. This result shows that the effective parameter based Eq. (3) cannot accurately predict failure when the micromechanisms of damage become complex, e.g. crack arrest after a considerable damage propagation. Nevertheless, the model is sufficiently capable of yielding fairly accurate estimates of ductility for different realizations of the microstructure.

3. Identification of critical failure regions in the microstructure

The sensitivity analysis in [7] can also be used to identify critical regions in the microstructure, where damage is expected to nucleate. The weakest regions are determined using a criterion based only on local volume fraction of inclusions and clustering, i.e. on the morphological parameter \tilde{f} . Eq. (3) cannot be used for this assessment due to the lack of knowledge of loading direction. Among the different locations identified as having a high level of clustering, ductile damage nucleation and propagation will occur at those locations, where large inclusions are favorably oriented for cracking. The microstructure of Fig. 4 is analyzed to demonstrate the capabilities of \tilde{f} for the identification of critical regions. The rectangular region has horizontal and vertical dimensions of $147 \mu\text{m} \times 125 \mu\text{m}$ and \tilde{f} is computed throughout the microstructure. Since the cluster contour index and local particle volume fraction are nonlocal statistics, each point considered must correspond to a square region over which these are computed. The size of this region is $15 \mu\text{m} \times 15 \mu\text{m}$ for the results shown in Fig. 5. This dimension is arrived at by a convergence study.

The contour plot of Fig. 5 shows four regions with high intensity that are identified as critical. These regions are circled in Fig. 4 and labeled. Regions R1 and R2 contain large inclusions and damage is expected to initially nucleate in these regions. Regions R3 and R4 may subsequently damage depending on the redistribution of micro-stresses. In-situ observations made during a SEM bending test at Ford Research Laboratory are shown in Fig. 6. Fig. 6a shows that damage at the onset of strain localization and final failure is mainly concentrated in regions R1, R2, and R4. A careful comparison of the Figs. 4 and 6a reveals that inclusion cracking has also occurred in region R3 prior to the final fracture. This confirms that \tilde{f} is an effective parameter for extracting critical regions in the microstructure. A comparison of the contour plot of Fig. 5 with one obtained using the local area fraction alone (not shown here) has shown that while \tilde{f} is able to clearly identify four critical regions, area fraction alone can only identify region R2. Both volume fraction and clustering are necessary determinants of failure initiation. In the absence of a sensitivity study, the product of volume fraction V_f and contour index ι may be used instead of \tilde{f} , as was proposed in [13]. Unlike \tilde{f} , this product is not derived from micromechanics simulations and is somewhat ad-hoc. The corresponding contour plots (not shown here) have similarities with Fig. 5, but the four regions are much less pronounced.

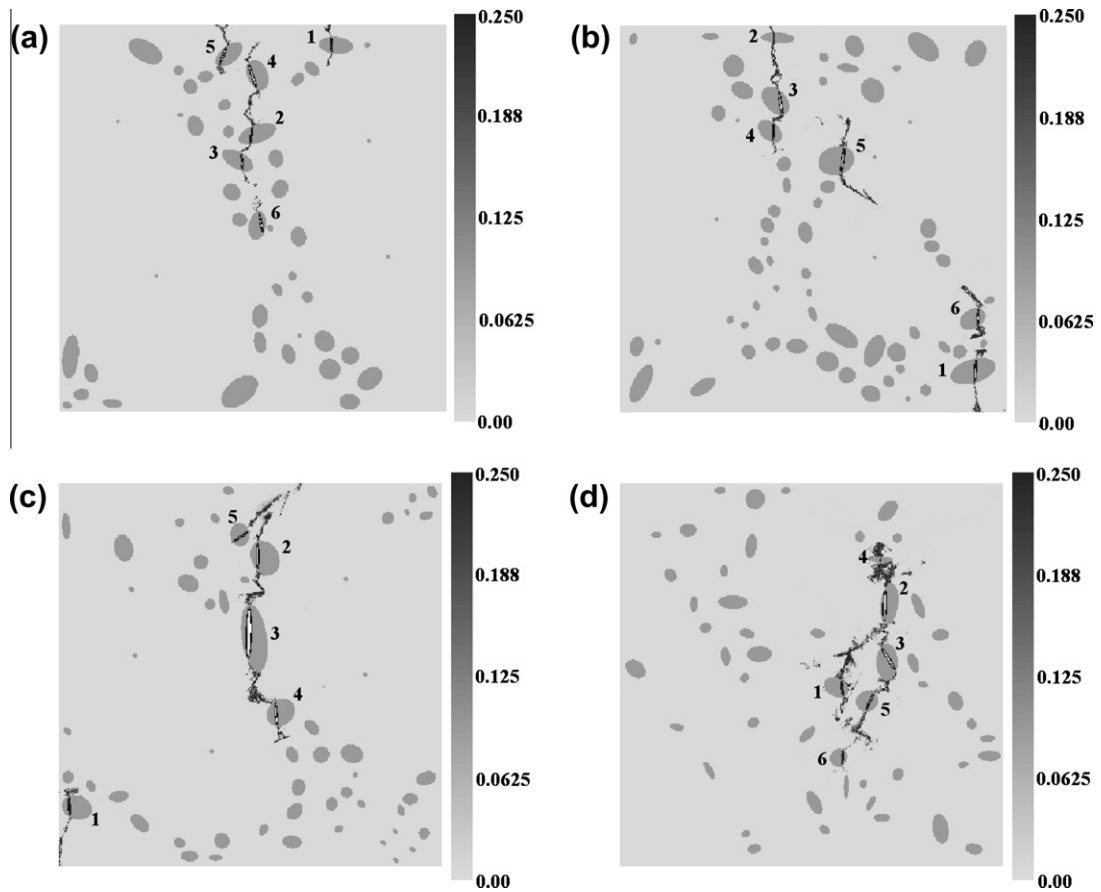


Fig. 3. Contour plots of microscopic void volume fraction (ductile crack path) at failure strain for four microstructural domains of a cast aluminum alloy A356: (a) microstructural domain 1, (b) microstructural domain 2, (c) microstructural domain 3 and (d) microstructural domain 4.

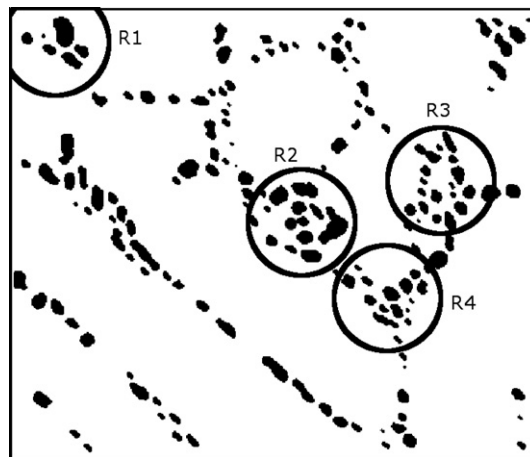


Fig. 4. Microstructure of a A356 cast aluminum alloy for identification of regions of low ductility. The horizontal and vertical dimensions are $147 \mu\text{m} \times 125 \mu\text{m}$ (Micrograph: Courtesy Ford Research Laboratory).

4. Dependence of ductility on applied strain rate

LE-VCFEM micromechanical analyses are conducted to investigate the effect of loading rates on strain to failure of the cast aluminum alloy A356. In [7] it has been shown that increasing the loading strain rate results in higher strain to failure for a

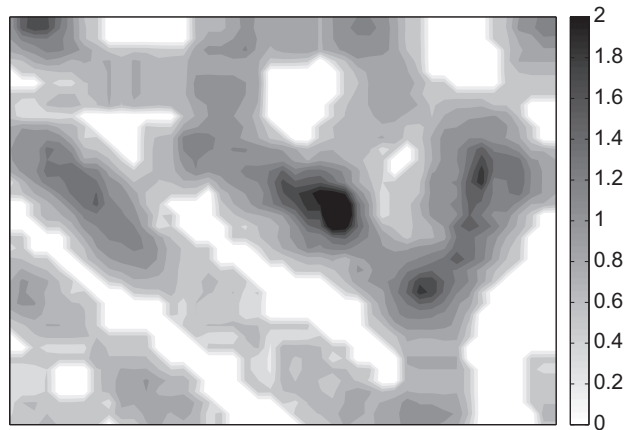


Fig. 5. Contour plot of \bar{f} for the microstructure of Fig. 4.

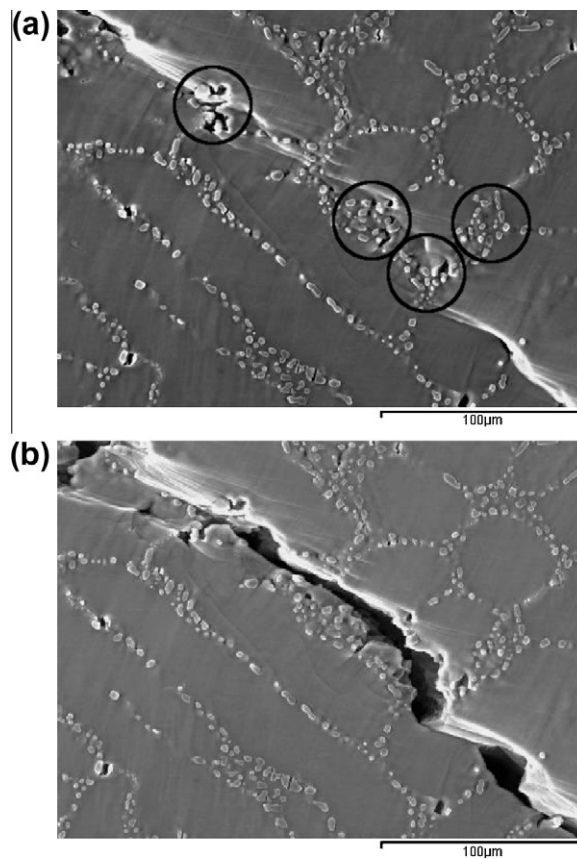


Fig. 6. In-situ observations of ductile fracture of a A356 cast aluminum alloy: (a) cracked particles at the onset of localization of damage and (b) final ductile failure after propagation of the crack through the aluminum matrix (Micrographs: Courtesy Ford Research Laboratory).

microstructural domain containing a single circular inclusion. The effect of applied strain rate on strain to failure of more complex, multi-inclusion microstructural domains is investigated in this section. Microstructural domains 3 and 4 in Section 2.2 are chosen for LE-VCFEM simulation due to the significant difference in their rate-independent ductile behavior as shown in Fig. 2. Material properties are those used for the sensitivity study in [7].

Three applied strain rates in the horizontal (x) direction under plane strain uniaxial tension conditions, are considered for each microstructural domain. For microstructural domain 3, the rates are:

- (1) $\dot{\epsilon}_{xx}^{(1)} = 1.56 \times 10^{-2} \text{ s}^{-1}$
- (2) $\dot{\epsilon}_{xx}^{(2)} = 1.25 \times 10^{-1} \text{ s}^{-1}$
- (3) $\dot{\epsilon}_{xx}^{(3)} = 5.00 \times 10^{-1} \text{ s}^{-1}$

while for microstructural domain 4, the rates are:

- (1) $\dot{\epsilon}_{xx}^{(1)} = 1.56 \times 10^{-2} \text{ s}^{-1}$
- (2) $\dot{\epsilon}_{xx}^{(2)} = 2.50 \times 10^{-1} \text{ s}^{-1}$
- (3) $\dot{\epsilon}_{xx}^{(3)} = 5.00 \times 10^{-1} \text{ s}^{-1}$

The microstructural domains are unconstrained in the vertical (y) direction and inertial effects are not considered. For comparison, the rate-independent response ($\gamma_0 \rightarrow \infty$) is also examined.

Figs. 7 and 8 show the microstructural domain averaged mechanical response for different loading rates. For higher applied strain rates, the strains to failure of both microstructural domains are significantly increased even though the high strain rates result in early inclusion cracking. This increase in ϵ_{fail} is attributed to stress redistribution that delays the evolution of plasticity in the matrix and reduces void nucleation and growth rates in the vicinity of the crack. The same observation has been made for a single circular inclusion microstructural domain in [7].

The responses of the two microstructural domains at a moderate applied strain rate of $1.56 \times 10^{-2} \text{ s}^{-1}$ are significantly different when compared to their rate-independent response. While microstructural domain 3 has an increased strain to failure, microstructural domain 4 sees its strain to failure reduced significantly in comparison with the rate-independent case. This shows that early inclusion cracking of microstructural domain 4 has led to premature void nucleation and growth in the

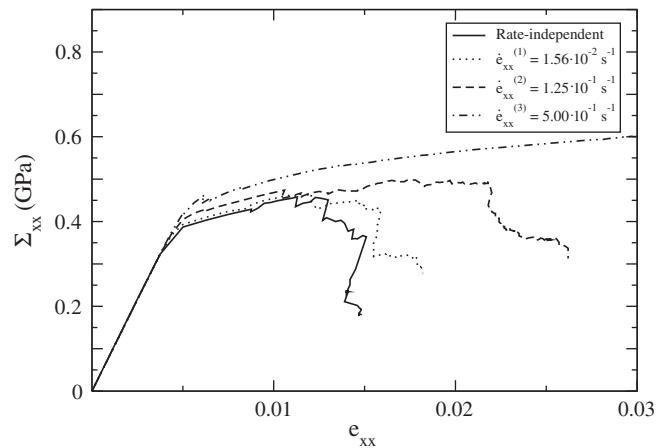


Fig. 7. Macroscopic stress–strain response for microstructural domain 3 at different uniaxial tensile strain rates.

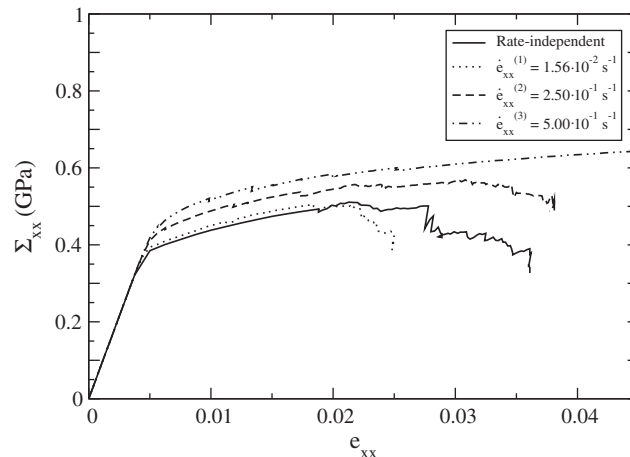


Fig. 8. Macroscopic stress–strain response for microstructural domain 4 at different uniaxial tensile strain rates.

aluminum matrix. This example conclusively demonstrates the importance of micromechanical simulations in ductility assessment of complex microstructures subjected to loading and environmental conditions, for which rate effects are important. No effective inference can be made based on the rate-independent material response since higher loading strain rates may result in an increase or a decrease of strain to failure.

5. Conclusions

This is the second of a two part paper on ductile fracture of heterogeneous metallic materials that investigates microstructural effects on rate-dependent ductile fracture in actual microstructures. Micromechanical analyses of microstructural domains of a cast aluminum alloy A356 are conducted by the locally enhanced Voronoi cell finite element method or LE-VCFEM. The model for strain to failure of microstructural domains having identical inclusions of same orientation, developed in [7], is extended in this sequel to actual microstructures by introducing effective morphological parameters of size, orientation and shape. LE-VCFEM simulations have been used to validate this new model for strain to failure of actual microstructures. Very good agreement on strain to failure is found between predictions of the model and results from direct LE-VCFEM simulations. This ductility model successfully captures the effects of clustering, volume fraction, orientation, shape and size of inclusions. The model works well for different loading directions with implicit material anisotropy. Results of the sensitivity study are also used to successfully identify critical regions in microstructural domain that are susceptible to incipient cracking. A parameter \hat{f} , combining the effects of volume fraction and clustering can identify these locations in the microstructure.

Finally, the effect of applied strain rates on ductile fracture is investigated. Higher strain rates result in early cracking of inclusions. The effect on strain to failure however strongly depends on the microstructural morphology in consideration. For very high rates, increase in ductility results from a delay of the matrix plastic response and a corresponding reduction in void evolution rate in the vicinity of a ductile crack. For a microstructural domain with higher rate-independent ductility, the strain to failure decreases by premature void nucleation and growth in the matrix due to early inclusion cracking when a moderate strain rate is applied. On the other hand, for a microstructural domain with lower rate-independent ductility, the strain to failure is increased with both moderate and high applied strain rates. Material failure behavior for complex microstructures, for which rate effects are important, is not so straightforward. The need for rigorous micromechanical analyses, featuring morphological, material and loading details, is strongly realized and emphasized for ductility assessment for these materials.

Acknowledgments

This work has been supported by the National Science Foundation NSF Div Civil and Mechanical Systems Division through the GOALI Grant No. CMS-0308666 (Program Director: Dr. G. Paulino), by the Department of Energy Aluminum Visions program through Grant No. A5997 and by the Army Research Office through Grant No. DAAD19-02-1-0428 (Program Director: Dr. B. Lamattina). This sponsorship is gratefully acknowledged. The authors are grateful to Drs. Steve Harris, John Allison, Xuming Su, and James Boileau of Ford Research Laboratory for invaluable discussions, use of micrographs and some material test data used in this paper. Computer support by the Ohio Supercomputer Center through Grant PAS813-2 is also gratefully acknowledged.

References

- [1] Caceres C, Davidson C, Griffiths J. The deformation and fracture behaviour of an Al–Si–Mg casting alloy. *Mater Sci Engng* 1995;A197:171–9.
- [2] Caceres C, Griffiths J, Reiner P. The influence of microstructure on the bauschinger effect in an Al–Si–Mg casting alloy. *Acta Mater* 1996;44:15–23.
- [3] Caceres C, Griffiths J. Damage by the cracking of silicon particles in an Al–7Si–0.4Mg casting alloy. *Acta Mater* 1996;44:25–33.
- [4] Caceres C. Particle cracking and the tensile ductility of a model Al–Si–Mg composite system. *Aluminum Trans* 1999;1:1–13.
- [5] Wang Q, Caceres C, Griffiths J. Damage by eutectic particle cracking in aluminum casting alloys A356/357. *Metall Mater Trans A* 2003;34A:2901–12.
- [6] Wang Q. Microstructural effects on the tensile and fracture behavior of aluminum casting alloys A356/357. *Metall Mater Trans A* 2003;34A:2887–99.
- [7] Paquet D, Ghosh S. Microstructural effects on ductile fracture in heterogeneous materials. Part I: sensitivity analysis with LE-VCFEM. *Engng Fract Mech* 2010;78:205–25.
- [8] Hu C, Ghosh S. Locally enhanced voronoi cell finite element model (LE-VCFEM) for simulating evolving fracture in ductile microstructures containing inclusions. *Int J Numer Meth Engng* 2008;76:1955–92.
- [9] Perzyna P. Fundamental problems in viscoplasticity. *Adv Appl Mech* 1966;9:243–377.
- [10] Chu CC, Needleman A. Void nucleation effects in biaxially stretched sheets. *J Engng Mater Technol* 1980;102:249–56.
- [11] Tvergaard V, Needleman A. Analysis of cup-cone fracture in a round tensile bar. *Acta Metall* 1984;32:157–69.
- [12] Tvergaard V, Needleman A. Effect of nonlocal damage in porous plastic solids. *Int J Solids Struct* 1995;32:1063–77.
- [13] Ghosh S, Valiveti D, Harris S, Boileau J. A domain partitioning based pre-processor for multi-scale modeling of cast aluminum alloys. *Model Simul Mater Sci Engng* 2006;14:1363–96.